IN-SITU MONITORING OF COMPOSITE FAILURE BY COMPUTING TOMOGRAPHY AND ACOUSTIC EMISSION

Sinan Kalafat[1], Andreea-Manuela Zelenyak[1] and Markus G. R. Sause[1]

[1] Experimental Physics II, Institute of Physics, University of Augsburg
Universitätsstrasse 1, D-86150, Augsburg, Germany
Email: markus.sause@physik.uni-augsburg.de, web page: http://www.uni-augsburg.de/exp2

Keywords: Computing tomography, Acoustic emission, Finite elements, Failure

ABSTRACT

After the initiation of failure in fibre reinforced composites, the evolution of damaged areas pose a major challenge to present failure theories. Therefore experimental methods such as in-situ computing tomography are highly valuable tools to detect the occurrence of first failure and to improve the understanding of failure progression. As recently been demonstrated by the use of synchrotron radiation sources, this approach leads to exciting new insights on the failure behaviour of fibre reinforced materials. In this study we present results of in-situ monitoring experiments using a carbon-fibre / epoxy system making use of a commercial computing tomography device achieving resolution down to 1.7 µm. The load frame is fully software controlled and has been optimized to yield a direct propagation path ready to detect acoustic emission signals as generated by the specimen under test. The signal detection uses flat with frequency sensors and a broad bandwidth of the acquisition equipment. The experiments are carried out as load-hold experiments with sufficient time intervals of hold to allow for specimen relaxation prior to scanning. The relevant time to stop the experiment and perform an imaging step is determined from simultaneous acoustic emission monitoring. Within this study, results of miniaturized samples subject to tensile testing transverse to the fibre axis are presented. The respective type of failure comprises one of the fundamental failure modes on the microscopic scale and is used to exemplify the experimental capabilities of the presented configuration in terms of resolution, contrast and defect detectability. Comparison is made between the detected acoustic emission signals and respective acoustic emission signal modelling using finite elements in the experimentally chosen 3D geometry. For the latter the crack surface is extracted from the computing tomography images and is directly used as source geometry for the numerical computation of the acoustic emission signal.

1 INTRODUCTION

Carbon fibre reinforced polymers (CFRPs) are a class of materials that show an extraordinary strength-to-weight and stiffness-to-weight ratio. However, the limited predictability of material failure requires a high margin of safety for the permissible design limits in construction of composite structures. Since global structural failure in composites is a consequence of a complex evolution of various microscopic failure mechanisms, to understand these evolution processes is key to understand global failure.

Several research groups demonstrated the use of X-Ray computing tomography (CT) to obtain information on the damage progress in fibre reinforced materials. The main advantage of X-Rays compared to light is their ability to penetrate the specimen and therefore to obtain volumetric information. The possibility to use computing tomography for visualization of internal damage states has become a standard method already. Some groups have been using synchrotron radiation in combination with in-situ loading stages to carry out volumetric imaging of miniature specimens under mechanical load [1]–[5]. Such microscopic imaging of the specimen allows to track the initiation of damage in the interior and to deduce the interaction between different failure mechanisms at increasing load levels. Other groups have adopted this analysis routine and investigated the failure of fibre reinforced materials under various load conditions carried out in-situ [1], [2], [4]–[11]. The term “in-situ” in this context typically refers to load-hold cycles with intermediate scanning. That way

damage is first introduced and existing damage states are kept under load. Stress relaxation effects have to be considered in general and creep effects of the matrix polymer have to be taken into account in particular. Moreover, there is currently no feasible technical solution to scale the method to allow specimen dimensions larger than the few millimetres of cross-section currently used.

In the same way as hearing complements vision, acoustic emission (AE) can act complementary to imaging methods in order to improve detection of failure. One major source for AE in CFRP is the initiation and growth of damage. Microscopically this relates to the generation and propagation of cracks inside the matrix material, along the interface between matrix and fibre or the rupture of fibre filaments and combinations of these individual contributions. Consequently, a combined measurement of acoustic emission signals during mechanical loading and CT inspection can be used to investigate composite failure.

Recent advances in AE also allow the forward prediction of the emitted AE signal of a specific source type by analytical methods [12] or by finite element modelling (FEM) [13]–[16]. The latter approach requires a thorough validation of the implementation to establish predictive capabilities for failure mechanisms occurring in fibre reinforced composites. To this end, recently an approach to establish such correlation based on optical microscopy was presented [16]. The present work demonstrates a similar approach in application to one of the fundamental failure modes in fibre reinforced composites, which is the occurrence of a matrix crack running transverse to the fibre direction.

2 EXPERIMENTAL

In order to combine in-situ CT scanning with AE measurements some modifications to existing load frames are required. In addition to the challenges faced by the load introduction and the geometrical stability, the generated AE signals need to be detected by an attached sensor system. For reasonable specimen sizes and miniaturized AE sensors these may be directly attached to the specimen.

But in order to achieve the highest scan resolution the specimen cross-section may typically approach dimensions of few mm², which does not allow a direct mounting of the substantially larger AE sensors. Hence, in such cases another approach is required to allow AE monitoring of specimen failure. To this end the load rigs presented in section 6.3 can be modified to include a waveguide to transfer the AE signal to an attached AE sensor. Figure 1 shows a 3D drawing of such a modified load rig used for tensile/compression testing with 180° of the PMMA tube removes to spot the interior arrangement. The top of the load rig has been modified to allow acoustic emission monitoring by using an AE sensor. The primary modification involves a slender wave-guide like design of the specimen fixture and an acoustic decoupling to the surrounding parts before reaching the sensor position. Using these modifications this allows a reasonable interpretation of the recorded AE signal without significant interference with signal reflections due to the surrounding components.

The specimens are fabricated as prepreg laminate using the carbon/epoxy system Sigrafil CE1250-230-39 following the curing cycle recommended by the manufacturer. Miniaturized samples of 1.9 mm × 1.7 mm × 2.8 mm length × width × height are cut from the laminates using a water cooled low-speed saw with precision diamond blade. Samples are attached to the aluminium load bars by an UHU Plus endfest 300 epoxy adhesive. Mechanical testing is carried out in displacement controlled mode using 0.2 mm/min displacement rate. Load-displacement curves are recorded by a software program. During loading and scanning AE measurements are performed using a KRNBB-PC type AE sensor with flat frequency response in the bandwidth ranging from 1 kHz to 3 MHz and a PCI-2 data acquisition card. All signals were amplified by 20 dB using a 2/4/6 preamplifier and recorded with 38 dB threshold and 10/80/300 settings for Peak-Definition-Time/Hit-Definition-Time/Hit-Lockout-Time using the software AEwin with 20 MHz sampling rate. For all configurations, a bandpass filter from 1 kHz to 3 MHz was used. For evaluation of the failure mode, a CT scan was performed after recording of an AE signal.

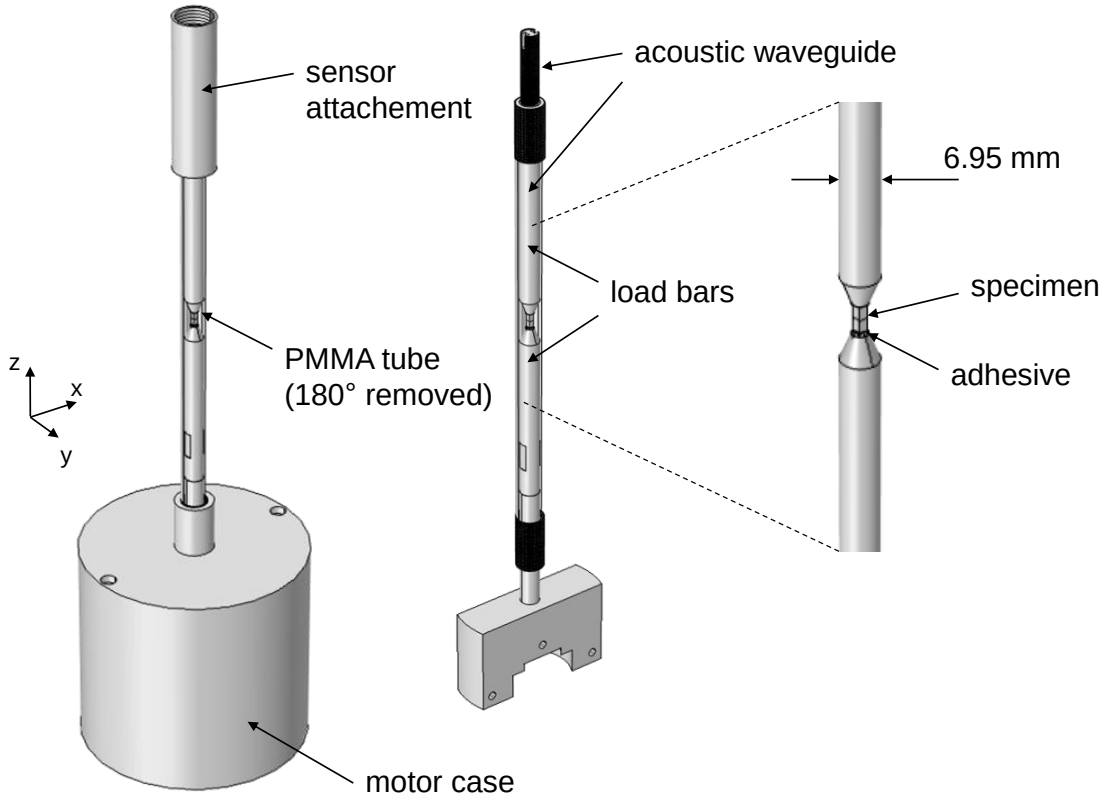

Figure 1: 3D drawing of in-situ load rig optimized for AE acquisition showing full device (left) and interior design with some parts removed (centre) as well as details of specimen attachment (right).

An exemplary CT scan after final failure of the specimen is shown in Figure 2 including details of the fracture plane. All scans were performed using a Nanotom 180 CT scanner using acquisition of 1000 images with detector exposure time of 1 s, tube voltage of 50 kV and tube current of 170 µA. Focus-object-distance and focus-detector-distance was chosen to yield a voxel size of 1.7 µm. 3D volumes were obtained by the "phoenix datos|x2 reconstruction" software and postprocessing was done by "VGStudio MAX". Given the 1.7 µm voxel resolution details of the fracture plane as well as inclusions (e.g. pores) in the bulk composite are readily visible. For tensile load transverse to the fibre direction, the failure mode is a matrix crack running through the full width of the specimen. Accordingly it is the movement of this fracture surface, which is the origin of the respective acoustic emission signal as indicated in Figure 2.

3 FEM MODELING

To accompany the experimental investigations, the specimen failure and the according acoustic emission release was modelled using FEM. The presented approach is an extension of the modelling approach base on cohesive zone elements presented in [16], [17]. Within the present study its application to composite materials is presented taking into account the anisotropic material properties as well as a 3D failure criterion. Moreover, the fracture surface was directly extracted from volumetric images.

The model itself consists of the 3D geometry already presented in Figure 1. To increase the computational efficiency, only geometries relevant for the problem are considered. To this end, the full geometry of Figure 1 is reduced to yield the reduced geometry of Figure 3. All computations are carried out within the "Structural Mechanics module" of Comsol Multiphysics following established routines for modelling of acoustic emission sources [13], [16], signal propagation [15] and detection [14]. Explicit modelling of the KRNBB-PC sensor is not necessary, since the voltage signal for this type is directly proportional to the out-of-plane displacement. Hence, the modelled AE signals are evaluated as displacement normal to the top surface of the load bar (z-direction) as indicated in Figure

3. All mesh settings were chosen to provide > 99% coherence as established in [15], with a maximal mesh size of 0.5 mm and respective refinement in regions of narrow details. The modelling procedure consists of two subsequent analysis steps. As first step, the model is subject to a static load applied along the z-axis direction with a value identical to the fracture load in the experiment (i.e. 200 N). In the second step, a transient analysis is performed allowing crack growth and AE release. As time step 10 ns were chosen to provide sufficient resolution during crack growth and signal propagation. The cohesive zone element approach requires a definition of an internal fracture plane. Assuming a planar fracture plane for this purpose might not take into account roughness or curvatures as existent in reality. Therefore, the present implementation uses a procedure to generate the internal fracture plane based on a CT scan of the specimen after failure.

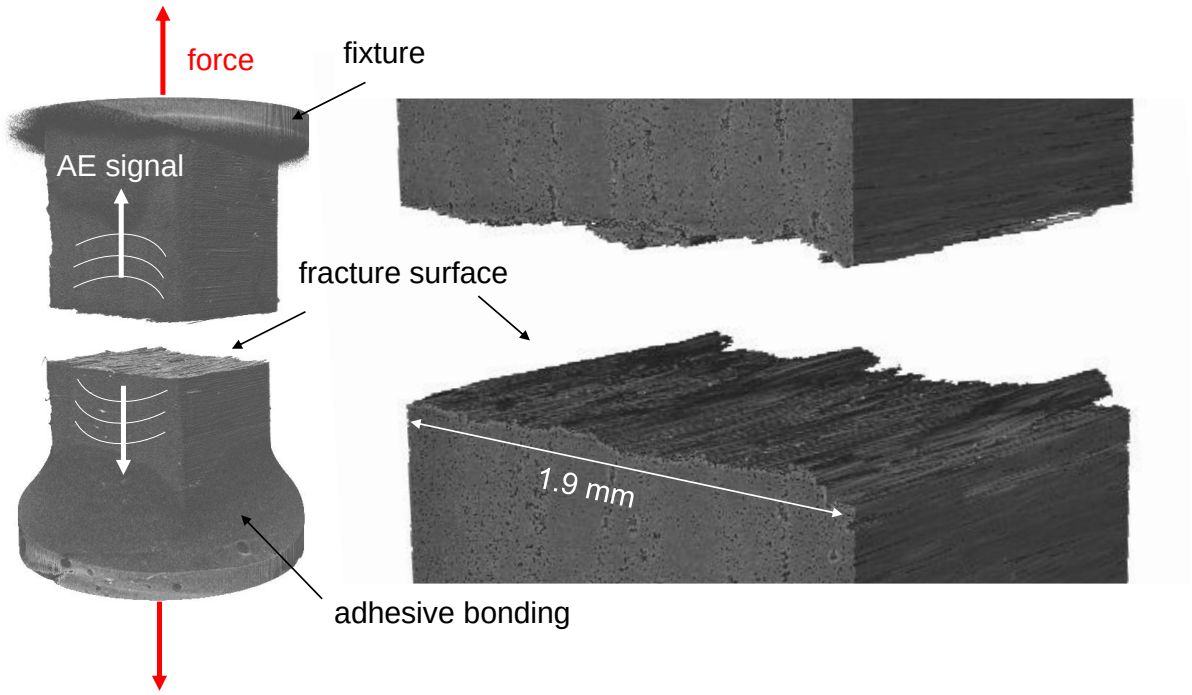

Figure 2: 3D scan of failure mode in in-situ load rig (left) and details of the fracture plane (right).

3.1 Extraction of fracture surface

As schematically shown in figure 3, the full procedure basically consists of three subsequent steps. As first step, the crack surface is extracted from a CT scan and digitized to yield a digital representation of the 3D-geometry. As second step, this digital object is imported to another software program for modification and refinement procedures. Finally, the resultant mesh is imported to a FEM program and embedded as CAD object for further processing. Although these steps are conceptually easy, the practical handling of the surface extraction, digitization and embedding comes with several challenges and may result in inaccuracies if carried out inappropriately.

First, the volume of the CT scan may be reduced to yield only the region of interest close to the fracture surface as basis for further processing as seen in Figure 3. The CT-scan should be of sufficient resolution and contrast, to allow proper image segmentation using gray-value based threshold techniques. For proper extraction of the crack surface, the selection of the segmentation threshold is of particular relevance and should be considered in detail when performing the segmentation step. Within "VGStudio MAX" it is possible to perform a surface extraction step using such threshold techniques. The obtained segmentation boundary can then be exported as stl-file format to yield a tessellated triangular surface for further processing. In this context, a "normal" level of detail was found to be appropriate for the surface extraction algorithm in "VGStudio MAX". Nevertheless, a high level of accuracy in this step may result in large files for further processing and may need adjustment subject to the extracted volume, scan resolution and computational capabilities for processing.

As next step, the obtained stl-file typically needs further processing before used in a FEM

environment. This is mostly due to issues arising from the tessellation algorithm applied to the extracted surface. First, there is a large likelihood, that the obtained fracture surface is not fully closed, which is caused by imperfections of the CT scan as well as the selected segmentation threshold. Such holes need to be closed, to yield an appropriate representation of the fracture surface. Second, the tessellation algorithm is likely to generate non-manifold faces and vertices in regions of geometric singularities (i.e. at the crack tip). Since these cause difficulties for generation of computational meshes these need to be removed as well. And finally, the presence of pores or crack bifurcations may cause isolated entities, which may be considered in FEM approaches, but may also lead to difficulties in mesh generations. Thus it was found to be useful to remove such isolated surfaces for further processing. Since all these operations are hardly implemented by manual mesh processing strategies, they require an appropriate environment to perform such stl-file modifications. To this end, the software platform "MeshLab" was used for processing and simplification of the extracted surface.

After import of the stl-file, the first step consists of a removal of isolated entities using the command "Remove Isolated pieces" applied to the imported mesh. Based on the selected option, this is used to remove all isolated objects depending on their diameter or number of faces. For further use within a FEM program, the topology of the obtained mesh may need some processing. Some of the mesh refinement strategies present in the next steps will require a mesh with 2-manifold edges. This means that each edge should be connected to exactly two neighbouring faces. Non-closed objects are typically 1-manifold (or even 0-manifold for plane edges) and objects containing artefact faces are 3- or more manifold. Before further processing, the vertices, edges or faces causing this lack of topological integrity of the surface need to be removed. Examples for such non 2-manifold edges are enclosed faces or overlapping faces. These are difficult to spot by bare eye, but are easy to to select and delete by using the "Select non Manifold Edges" filter. Careful removal without compromising the integrity of the geometry is used to yield a suitable mesh representation for further processing.

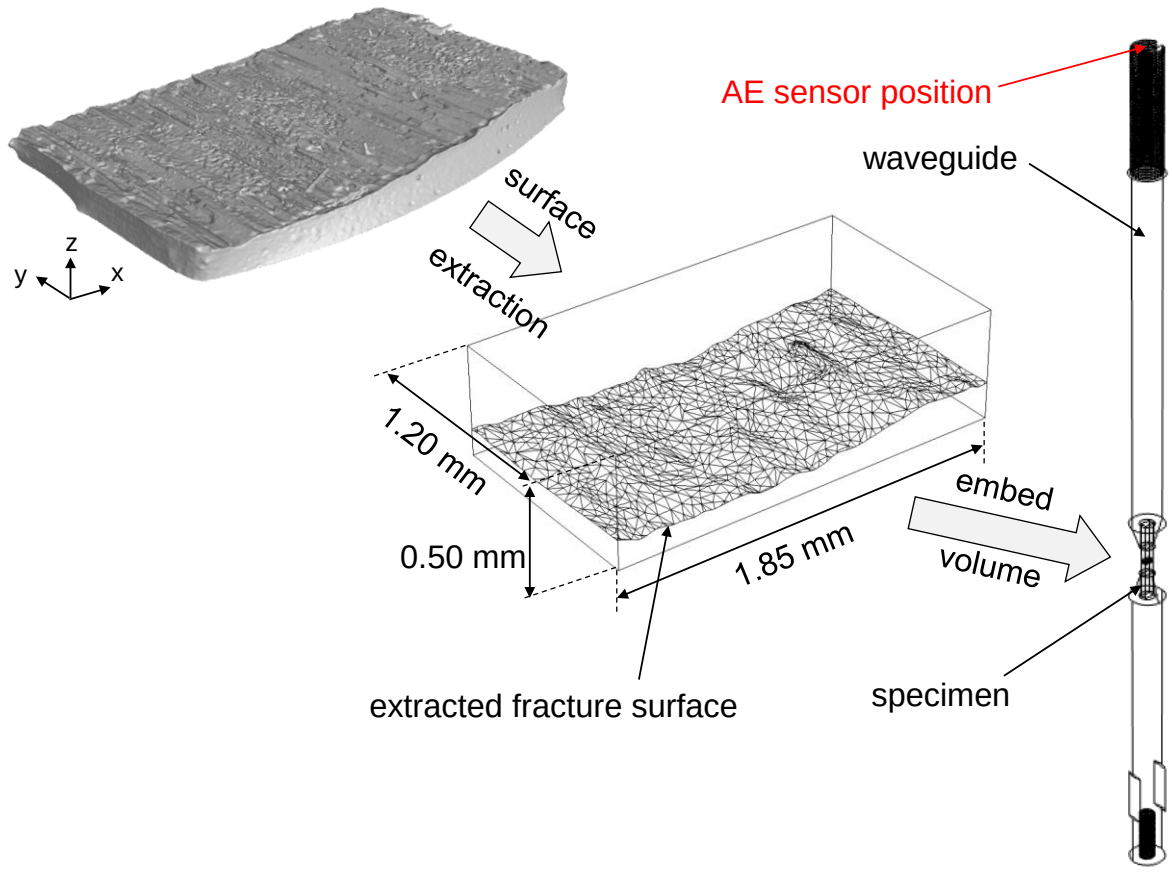

Figure 3: Scheme of procedure used to transfer CT-scan of fracture surface into FEM-model.

Subsequently, the mesh is subject to a simplification scheme. Among the different choices, the "quadratic based edge collapse strategy" option following the scheme of H. Hoppe was found to be particularly useful [18]. In all cases, key is to preserve the topology of the extracted surface and to avoid removal of geometric details, which are required for the computation result. The latter aspect is hard to determine at this stage, so the simplification routine should be evaluated in their impact on the computation results by comparing the results obtained by less simplified cases and by the desired level of simplification. Clearly, this step is used to increase the numerical efficiency of the modelling procedure and should thus be considered carefully to reach a satisfying level of detail, while keeping the numerical intensity at a minimum. Generated or existing structure holes are then filled using the "Fill holes" or "Close holes" command. As final step, the simplified and repaired surface is exported to another stl-file.

Within the FEM program "Comsol Multiphysics" stl-files may be imported during geometry creation. For the present case, only the fracture surface shown in Figure 3 was imported. The remaining parts of the specimen may either be imported from other CAD formats or are being generated directly within "Comsol Multiphysics". The imported crack surface was joined with a surrounding volume using a sequence of intersection and union commands to yield the volume shown in Figure 3. The so obtained volume was then embedded within the full 3D-geometry of the in-situ test stage as shown in Figure 3.

3.2 Implementation of failure criterion

The implementation of crack growth modeling in "Comsol Multiphysics" is performed using cohesive zone modeling following the detailed implementation described in [16]. The boundary condition "thin elastic layer" can be defined for an internal surface and is used to model transient crack growth. The stiffness vector $\boldsymbol{k}$ of this thin elastic layer is written in terms of the boundary coordinate system (t_1, t_2, n). Suitable values for the stiffness may be estimated from the Young's modulus E, the shear modulus G and the Poisson's ratio ν of an isotropic material as follows:

$$\boldsymbol{k} = \begin{pmatrix} k_{t1} \\ k_{t2} \\ k_n \end{pmatrix} \tag{1}$$

$$k_{t1} = k_{t2} = \frac{G}{t_h} \tag{2}$$

$$k_n = \frac{E(1-\nu)}{t_h(1+\nu)(1-2\nu)} \tag{3}$$

The parameter t_h is an effective thickness associated with the thin elastic layer. The thickness value t_h is chosen sufficiently small (i.e. < 1 nm), so that the value of $\boldsymbol{k}$ has negligible influence on the overall compliance of the model. For the present case $E = C_{22}$, $G = C_{44}$ and $\nu = \nu_{12}$ was chosen. Although this yields only a first order approximation of the values, a proper choice of t_h was found to be much more relevant to yield negligible compliance of the closed crack surface.

To model crack propagation, the stiffness vector is multiplied by a degradation function $\check{C}(\boldsymbol{r})$ evaluated as a function of the position on the fracture surface $\boldsymbol{r}$. For the present case, Puck's inter-fibre failure criterion ($PUCK$) was implemented following [19]–[21]**.** In its full form, for the case studied herein ($\sigma_n \geq 0$), this is written as:

$$PUCK = \sqrt{\left[\left(\frac{1}{R_{\perp}^{+}} - \frac{p_{\perp\psi}^{+}}{R_{\perp\psi}^{A}}\right)\cdot\sigma_n\right]^2 + \left(\frac{\tau_{nt}}{R_{\perp\perp}^{A}}\right)^2 + \left(\frac{\tau_{n1}}{R_{\perp\parallel}}\right)^2} + \frac{p_{\perp\psi}^{+}}{R_{\perp\psi}^{A}}\cdot\sigma_n \tag{4}$$

For technical reasons, the "Comsol Multiphysics" environment also requires an additional ordinary differential equation to be defined on the fracture surface. This is to track the historic maximum value

$PUCK_{max}$ of $PUCK$. Therefore, the current implementation evaluates, whether the fracture condition is fulfilled in the present time step i or was fulfilled in any previous time step.

Therefore the degradation function is written in terms of Puck's inter-fibre failure criterion as follows:

$$\check{C}(\boldsymbol{r}) = \begin{cases} 1 & if \quad \max(PUCK_{max}(\boldsymbol{r}), PUCK(\boldsymbol{r})) < 1 \\ 0 & if \quad \max(PUCK_{max}(\boldsymbol{r}), PUCK(\boldsymbol{r})) \geq 1 \end{cases} \tag{5}$$

The advantage of the present description compared to other formulations for acoustic emission source models is the access to experimental parameters. In the proposed model, crack growth and acoustic emission is solely defined by the macroscopic loading condition and the failure criterion used. In particular, no explicit source function comprising internal forces or rise-times are necessary to initiate an AE signal, thus reducing the ambiguity in AE source modeling. All material properties used in the model are listed in Table 1.

	Density [kg/m³]	Poisson-Ratio	Elasticity Constants [GPa]	$R_{\perp}^{+}$ [MPa]	$R_{\perp\perp}^{A}$ [MPa]	$R_{\perp\parallel}$ [MPa]	$p_{\perp\psi}^{+}$
Sigrafil CE 1250-230-39	1500	-	C_{11}=131.0 C_{12}= C_{13}=3.7 C_{22}= C_{33}=8.1 C_{23}=3.1 C_{44}=2.1 C_{55}= C_{66}= 6.1	54	80	80	0.3
Aluminium	2700	0.33	69.0	-	-	-	-
Adhesive	1140	0.38	2.8	-	-	-	-

Table 1: Material properties used for FEM modeling.

4 RESULTS

Based on the proposed modelling approach, results of crack progression and the according AE signal excitation are presented in the section 4.1. Subsequently, in section 4.2 the model results are compared to experimental results to demonstrate the validity of the FEM approach.

4.1 Analysis of failure mode and generation of acoustic emission

Due to the presence of the static load in z-direction, a static displacement field exists within the specimen. As pointed out in the previous section this static load and displacement field is used as initial boundary condition for a second computation step. This initiates the transient degradation of the stiffness vector of the thin elastic layer based on the evaluation of Puck's inter-fibre failure criterion. A sequence of images during the crack propagation is shown in Figure 4.

The false colour range of the degradation function $\check{C}(\boldsymbol{r})$ indicates the extension of the crack by red areas, while blue colours resemble areas, where the material is still in contact. The images show the state of crack growth between t = 0.2 µs and t = 1.2 µs. The initiation point is located at the lower left corner of the embedded fracture plane. The initiation is solely owed to the stress concentration at this edge based on the 3D topology of the fracture plane and the applied load level. After initiation, the crack grows along the fracture plane due to the stress concentration at the crack front. The extension of the fracture plane is driven by the roughness of the fracture surface and the velocity of crack growth approaches the speed of a Rayleigh wave, which is the general limit of crack propagation velocity.

Due to the orientation of the local stress components, the newly formed fracture surface are subject to a dominant Mode-I type load situation. This causes a crack opening during propagation of the crack and the according movement of the fracture surfaces constitutes the actual source mechanism for AE release. The initiation of the dynamic motion of the fracture planes are conveniently visualized using diagrams of the acoustic velocity magnitude to visualize the birth of the AE signal around the crack. As seen from Figure 5, the near-field of this crack type consists of a dominant radiation perpendicular

to the crack surfaces, which extends along the x- and y-axis during the progression of the crack. After t = 3.0 µs the first reflections at the edges of the small specimen superimpose to the emitted waves of the source. Thus it is more convenient to adapt the false-color scale and observe the signal spreading in the attached waveguide.

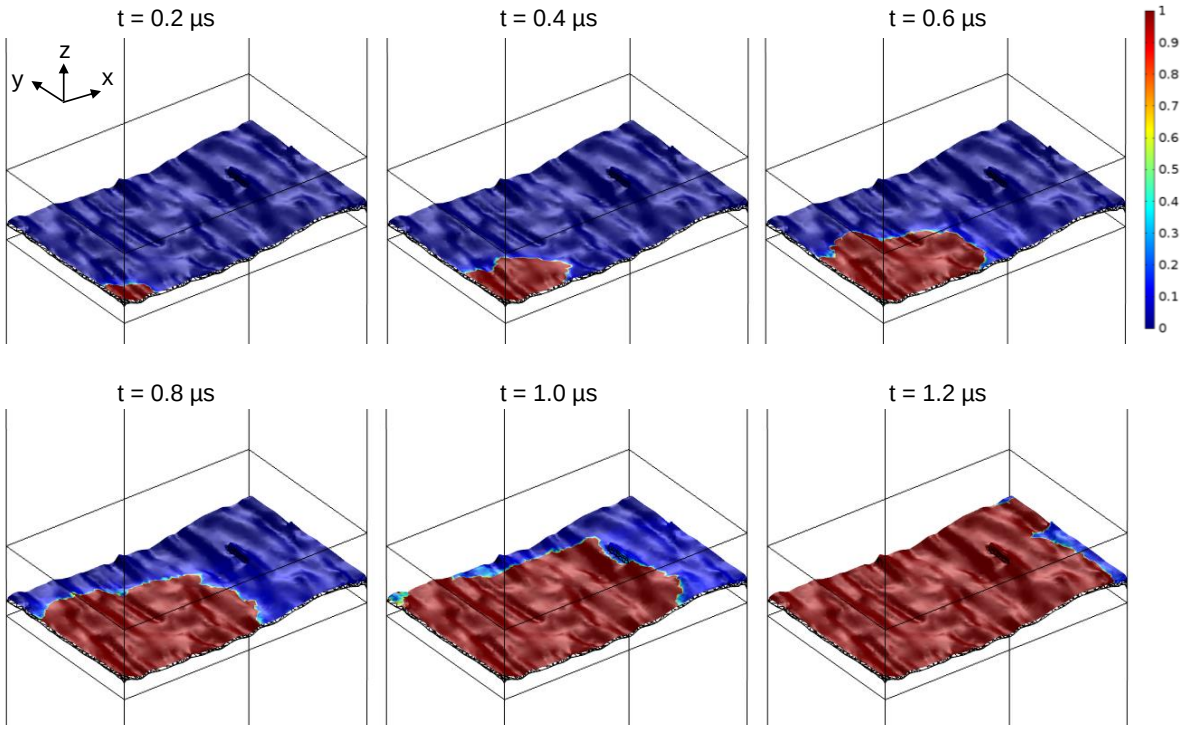

Figure 4: Calculated crack growth in in-situ tensile test with fibre orientation perpendicular to load axis at distinct time intervals with false colour range to indicate the value of the degradation function.

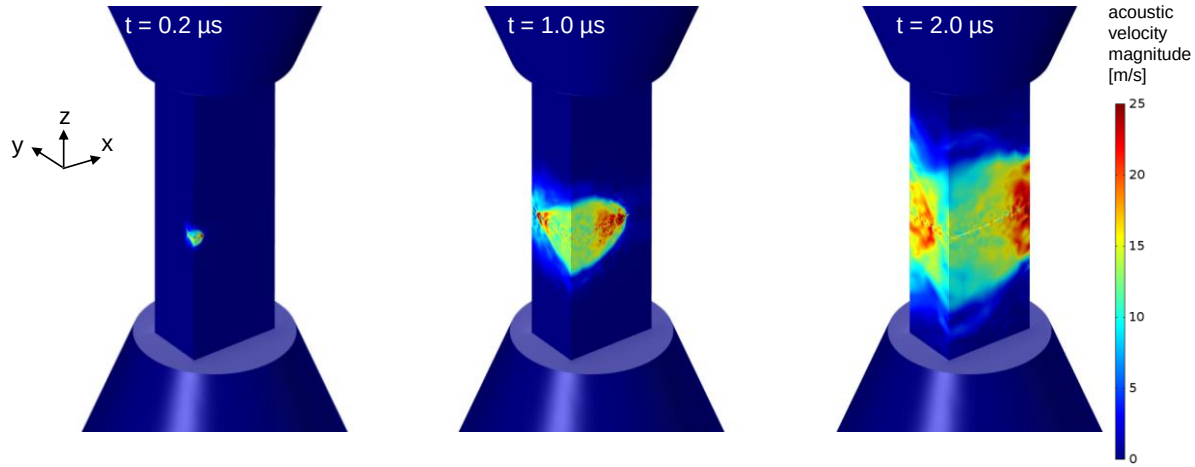

Figure 5: Plot of acoustic velocity magnitude during and after crack growth.

Within the waveguide (i.e. tensile bar) the incident waves are converted into guided waves, which propagate towards the AE sensor position. As seen from the acoustic velocity fields in Figure 6 at six distinct time steps, there are several guided wave modes visible within the waveguide. The two dominant wave packages were identified as primary and secondary F(1,0) modes by means of time-frequency analysis using Choi-Williams diagrams and dispersion curves calculated using [22] for the 6.95 mm aluminum rod [23], [24].

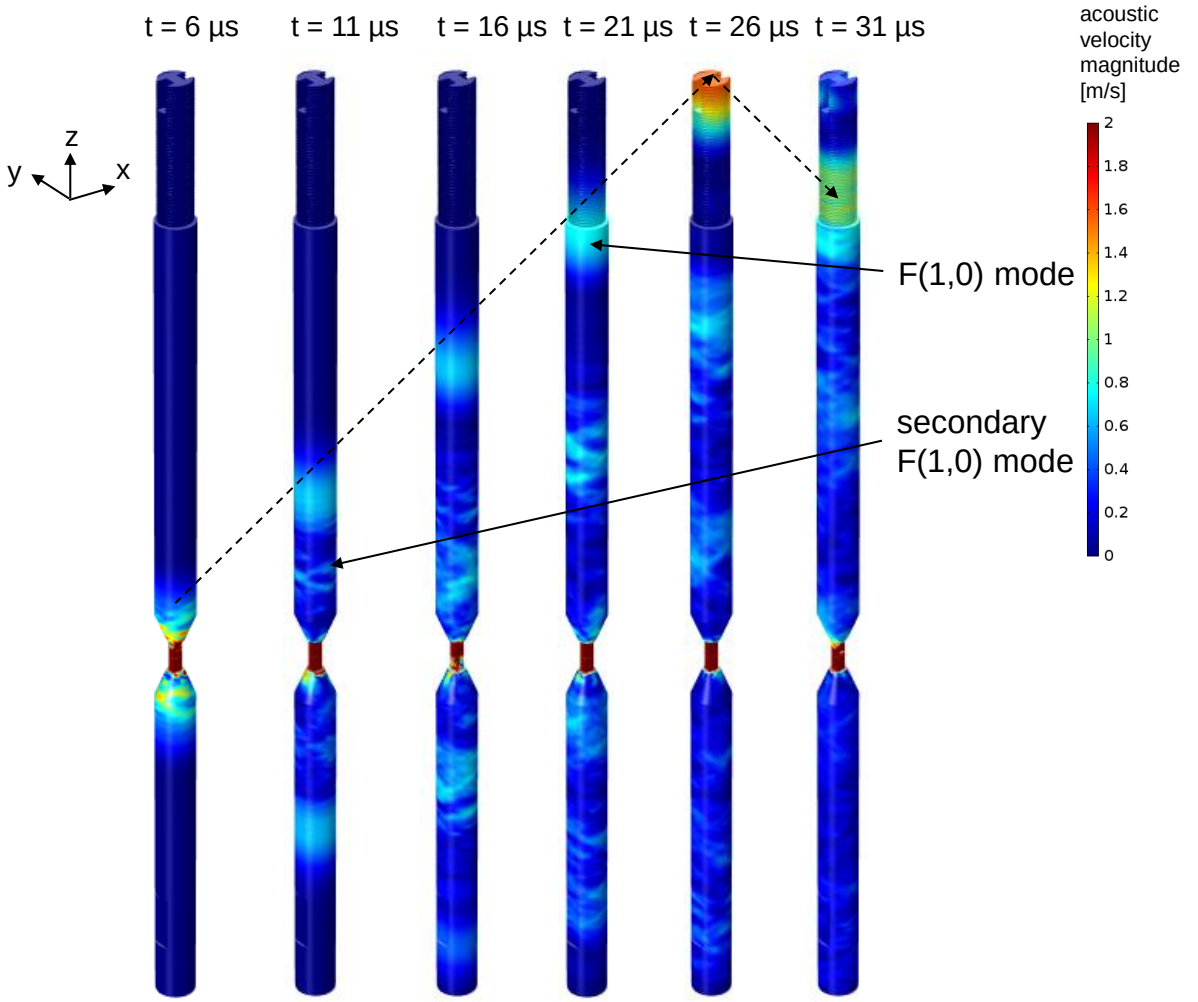

Figure 6: Plot of acoustic velocity magnitude during signal spreading in waveguide geometry.

4.2 Comparison of FEM results and experimental data

The displacement normal to the top surface of the waveguide is evaluated as AE signal and is shown in Figure 7 for the calculated duration of t = 60 µs. For comparison, the respective experimental AE signal obtained for the investigated fracture surface is shown in Figure 7 as well. The behaviour of the experimentally used KRNBB-PC sensor can readily be estimated as flat frequency response with constant conversion factor of 6 kV/m also accounting for the preamplifier gain. Thus the modelled sensor voltage may directly be compared to the experimental sensor voltage. In addition, the modelled signal was filtered by a 6th order Butterworth high-pass of 1 kHz to confirm with the bandwidth limitations of the experimental setup. As seen from the good quantitative agreement between both signals, the proposed model setup is able to describe the generated AE signal very well. Since the approach presented herein is an extension of previous research [16], [17], this finding is not surprising. Some differences arise with respect to the number and position of dips after 25 µs. Based on visual observations of the signal propagation path, this is likely owed to interactions with parts not included within the model, which cause additional reflections arriving at the sensor position after the first wave mode has passed beyond the sensor position (cf. Fig. 6). Since the experimental signal will also move into the sensor and will interact with the surrounding metallic sensor fixture this will contribute to the shape of the signal to a certain extent. However, except for the first rise in the signal, the shape is

dominated by the experimentally used bandpass filter, which causes the sharp falling slope between 20 µs and 40 µs and the rising slope from 40 µs on.

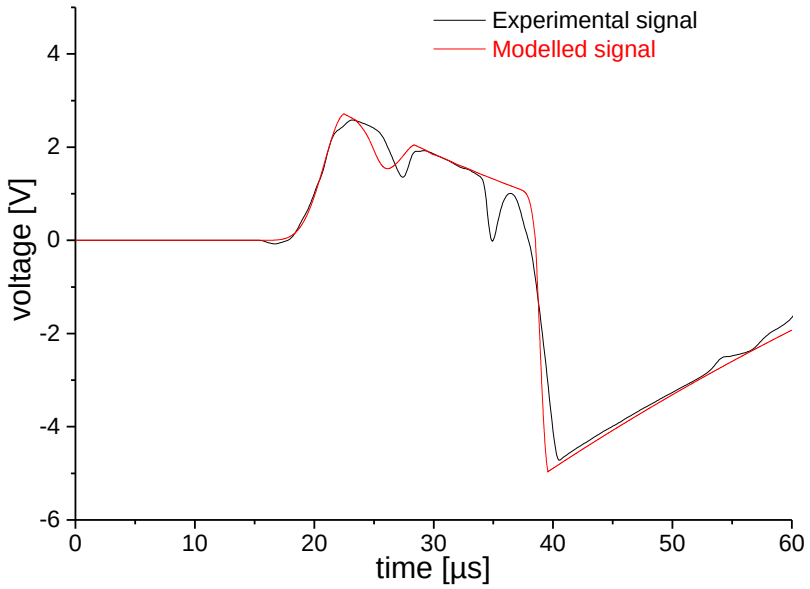

Figure7: Comparison of experimental AE signal and modelled AE signal.

5 CONCLUSIONS

With the present modelling approach an improved description of the acoustic emission release due to the process of crack formation in fibre reinforced materials is possible. The insight gained by such modelling work aids in the interpretation of the physical processes during crack formation and allows assessing the impact of the material properties on the excited acoustic emission signals. The combination with in-situ computing tomography approaches allows to validate such modelling approaches on the microscopic scale. The extraction of fracture surfaces from 3D computing tomography images presents a promising new approach to be used in combination with cohesive zone modelling. The presented tools will allow an extension of the modelling approach to larger specimens with complex failure modes. This will be key to understand the formation of acoustic emission signals in more complex damage scenarios.

REFERENCES

[1] M. Stampanoni, A. Groso, A. Isenegger, G. Mikuljan, Q. Chen, A. Bertrand, S. Henein, R. Betemps, U. Frommherz, P. Böhler, D. Meister, M. Lange, R. Abela, and P. Boehler, “Trends in synchrotron-based tomographic imaging: the SLS experience,” in *Developments in X-Ray Tomography V*, 2006, vol. **6318**, p. 63180M–63180M–14.

[2] A. E. Scott, M. Mavrogordato, P. Wright, I. Sinclair, and S. M. Spearing, “In situ fibre fracture measurement in carbon-epoxy laminates using high resolution computed tomography,” *Compos. Sci. Technol.*, vol. **71**, no. 12, pp. 1471–1477, 2011.

[3] A. E. Scott, M. Clinch, W. Hepples, N. Kalantzis, I. Sinclair, and S. M. Spearing, “Advanced micro-mechanical analysis of highly loaded hybrid composite structures,” in *ICCM 17 - 17th International Conference on Composite Materials*, 2009.

[4] F. Ritschel, M. Zauner, S. J. Sanabria, M. G. R. Sause, B. R. Pinzer, a. J. Brunner, M. Stampanoni, and P. Niemz, “Damage evolution in wood: Synchrotron based micro-tomography as complementary evidence for interpreting acoustic emission behavior,” *Holzforschung*, 2014.

[5] A. Groso, R. Abela, and M. Stampanoni, “Implementation of a fast method for high resolution phase contrast tomography,” *Opt. Express*, 2006.

[6] A. E. Scott, W. Hepples, N. Kalantzis, P. Wright, M. N. Mavrogordato, I. Sinclair, and S. M. Spearing, "High resolution damage detection of loaded carbon/epoxy laminates using synchrotron radiation computed tomography," in *18th International conference on composite materials*, 2011, pp. 1–6.
[7] E. Maire, V. Carmona, J. Courbon, and W. Ludwig, "Fast X-ray tomography and acoustic emission study of damage in metals during continuous tensile tests," *Acta Mater.*, vol. **55**, no. 20, pp. 6806–6815, 2007.
[8] A. E. Scott, I. Sinclair, S. M. Spearing, M. N. Mavrogordato, and W. Hepples, "Influence of voids on damage mechanisms in carbon/epoxy composites determined via high resolution computed tomography," *Compos. Sci. Technol.*, vol. **90**, pp. 147–153, 2014.
[9] G. Borstnar, M. N. Mavrogordato, I. Sinclair, and S. M. Spearing, "Micro - Mechanistic Analysis of in Situ Crack Growth in Toughened Carbon / Epoxy Laminates To Develop Micro - Mechanical Fracture Models," in *ECCM16 - 16th European Conference on Composite Materials*, 2014, no. June, pp. 22–26.
[10] R. Brault, a. Germaneau, J. C. Dupré, P. Doumalin, S. Mistou, and M. Fazzini, "In-situ Analysis of Laminated Composite Materials by X-ray Micro-Computed Tomography and Digital Volume Correlation," *Exp. Mech.*, vol. **53**, no. 7, pp. 1143–1151, 2013.
[11] A. J. Moffat, P. Wright, J. Y. Buffière, I. Sinclair, and S. M. Spearing, "Micromechanisms of damage in 0° splits in a [90/0]s composite material using synchrotron radiation computed tomography," *Scr. Mater.*, vol. **59**, no. 10, pp. 1043–1046, 2008.
[12] P. D. Wilcox, C. K. Lee, J. J. Scholey, M. I. Friswell, M. R. Wisnom, and B. W. Drinkwater, "Progress Towards a Forward Model of the Complete Acoustic Emission Process," *Adv. Mater. Res.*, vol. **13–14**, pp. 69–75, 2006.
[13] M. G. R. Sause and S. Horn, "Simulation of acoustic emission in planar carbon fiber reinforced plastic specimens," *J. Nondestruct. Eval.*, vol. **29**, no. 2, pp. 123–142, 2010.
[14] M. Sause, M. Hamstad, and S. Horn, "Finite element modeling of conical acoustic emission sensors and corresponding experiments," *Sensors Actuators A Phys.*, 2012.
[15] M. G. R. Sause, M. A. Hamstad, and S. Horn, "Finite element modeling of lamb wave propagation in anisotropic hybrid materials," *Compos. Part B Eng.*, vol. 53, pp. 249–257, 2013.
[16] M. G. R. Sause and S. Richler, "Finite Element Modelling of Cracks as Acoustic Emission Sources," *J. Nondestruct. Eval.*, vol. **34**, no. 1, 2015.
[17] H. Hoppe, "New Quadric Metric for Simplifying Meshes with Appearance Attributes," in *10th IEEE Visualization 1999 Conference (VIS '99)*, 1999.
[18] H. M. Deuschle and A. Puck, "Application of the Puck failure theory for fibre-reinforced composites under three-dimensional stress: Comparison with experimental results," *J. Compos. Mater.*, vol. **47**, no. 6–7, pp. 827–846, 2013.
[19] A. Puck and H. Schürmann, "Failure analysis of FRP laminates by means of physically based phenomenological models," *Compos. Sci. Technol.*, vol. **62**, no. 12–13 SPECIAL ISSUE, pp. 1633–1662, 2002.
[20] A. Puck and M. Mannigel, "Physically based non-linear stress-strain relations for the inter-fibre fracture analysis of FRP laminates," *Compos. Sci. Technol.*, vol. **67**, no. 9, pp. 1955–1964, 2007.
[21] F. Seco and A. R. Jiménez, "Modelling the Generation and Propagation of Ultrasonic Signals in Cylindrical Waveguides," in *Ultrasonic Waves*, Intech Open Access Publisher, 2012, pp. 1–28.
[22] M. A. Hamstad, "Comparison of Wavelet Transform and Choi-Williams Distribution to Determine Group Velocities for Different Acoustic Emission Sensors," *J. Acoust. Emiss.*, vol. **26**, pp. 40–59, 2008.
[23] H.-I. Choi and W. Williams, "Improved Time-Frequency Representation of Multicomponent Signals Using Exponential Kernels," *IEEE Trans. Acoust. Speech Signal Process.*, vol. **37**, no. 6, pp. 862–872, 1989.